

Impact of echo broadening effect on active range-gated imaging

Xinwei Wang (王新伟)*, Yan Zhou (周燕), and Yuliang Liu (刘育梁)

Optoelectronic System Laboratory, Institute of Semiconductors, Chinese Academy of Sciences, Beijing 100083, China

*Corresponding author: wangxinwei@semi.ac.cn

Received March 2, 2012; accepted April 25, 2012; posted online August 3, 2012

Analytical formulas and experimental proof of the echo broadening effect in active range-gated imaging, including atmospheric interference, currently exist. We investigate the impact of this effect on target detection. Our research demonstrates that the echo broadening effect affects the energy profile of the depth of view and collects only part of the signals of targets in head and tail zones. Under bad weather conditions, the effect weakens the signal-to-noise ratio (SNR) of images, especially in cases with large laser pulse width. Fortunately, by modifying the laser pulse width, the effect can be controlled. These results are valuable to the applications of active range-gated imaging.

OCIS codes: 110.4280, 110.0113, 120.0280.

doi: 10.3788/COL201210.101101.

Active range-gated imaging has been widely used in 3D imaging^[1–5], underwater imaging^[6,7], security surveillance^[8], and 4D imaging^[9], because it can give high-quality range images by suppressing atmospheric backscattering. This technique is realized by the synchronization of a pulsed laser and a gated camera. However, in range-gated imaging, the convolution of the laser pulse and the gate pulse impacts the energy profile of the depth of view (DOV)^[7,10]. To emphasize this impact and resolve the confusion about the DOV being directly determined by gate time with laser pulse width ignored, Wang *et al.*^[11] established the concept of range-gated echo broadening effect (EBE) in 2009. Much excellent fundamental research about active range-gated imaging has been performed^[10,12,13], but experimental proof of the EBE and data regarding its impact on target detection remain limited. The objective of this letter is thus to investigate this effect and its impact in theory and practice.

In an active range-gated imaging system, a pulsed laser is used to illuminate targets. When the laser pulse travels in air, it is reflected by objects in the field of illumination to form echo signals propagating toward the imaging system (Fig. 1(a)). The camera gate of the system opens with the predefined gate time at the predefined delay time, but it is kept closed at all other times to avoid laser radiation from unwanted ranges. The delay time is $2R/c$, where c is the speed of light in vacuum and R is the beginning range of the region of interest (Fig. 1). In this letter, the atmospheric refractive index is approximated as 1. The laser pulse width is given as t_L and thus has a pulse length $t_L c$ on the way of propagation. At the instance that the echo signal of person T1 induced by the leading edge of the laser pulse reaches the tree at range r , where $R - t_L c/2 < r < R$, the tree will have been exposed to laser radiation for a certain duration $t_L - 2(R - r)/c$ (Fig. 1(b)) and the “person signal” will be then reinforced by the laser radiation from the tree. When the gate opens, the person signal of T1 and part of the tree signal are both received by the camera. Under this effect, objects lying in the range interval of

$R - t_L c/2$ to R can all be imaged. At the critical state that the gate closes after the integration period t_g , the echo signal from the target T2 at $R + t_g c/2$ only reaches the gate with a zero value due to the zero illumination of the leading edge of the laser pulse to T2 (Fig. 1(c)). Finally, the DOV is expanded from $t_g c/2$ to $(t_L + t_g)c/2$. The above-mentioned phenomenon is the range-gated EBE, which can be described by the convolution of the laser pulse and the gate pulse in theory. The radiant energy $E(r)$ received by the imaging system is the incident radiant energy of the laser pulse integrated during the gate time:

$$E(r) = \int_0^{\infty} P(t - 2r/c)G(t - \tau)dt, \quad (1)$$

where τ is the delay time between the laser pulse and the gate pulse, $P(t)$ is the laser function, and $G(t)$ is the gate function. Considering atmospheric attenuation and other temporal and spatial factors, such as system repetition frequency, laser beam divergence, and target reflection property, among others, Eq. (1) can be modified as

$$E(r) = \frac{f_L}{f_{\text{CCD}}} \frac{\rho}{\pi} \frac{A_t}{A_L} \frac{A_r}{r^2} \exp(-2\sigma r) \eta_t \eta_r \cdot \int_0^{\infty} P(t - 2r/c)G(t - \tau)dt, \quad (2)$$

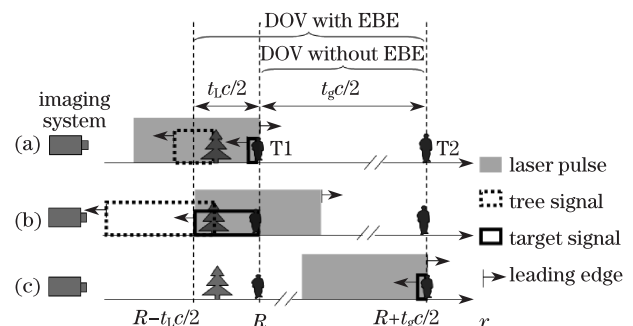


Fig. 1. Range-gated EBE.

where f_L is the laser pulse repetition frequency; f_{CCD} is the frame rate of CCD; η_r and η_t are the transmission efficiencies of receiving and transmitting optical systems, respectively; ρ is the target reflection coefficient; A_r is the receiver area; A_t is the effective laser cross-section; A_L is the illuminated area; σ is the atmospheric total extinction coefficient. Correspondingly, the energy of atmospheric backscattering $E_s(r)$ can be given as

$$E_s(r) = \frac{f_L}{f_{\text{CCD}}} \eta_t \eta_r \frac{\sigma A_r}{8\pi} \int_0^\infty \int_{R-t_L c/2}^{R+t_g c/2} \cdot P\left(t - \frac{2r}{c}\right) G(t - \tau) \frac{\exp(-2\sigma r)}{r^2} dt dr. \quad (3)$$

If the laser pulse and the gate are in rectangular form, then

$$G(t - \tau) = \begin{cases} G & (0 \leq t - \tau \leq t_g) \\ 0 & \text{otherwise} \end{cases}, \quad (4)$$

$$P(t - 2r/c) = \begin{cases} P_{\text{peak}} & (0 \leq t - 2r/c \leq t_L) \\ 0 & \text{otherwise} \end{cases}, \quad (5)$$

where G is the gain of the camera and P_{peak} is the peak power of the pulsed laser. The simulation result of Eq. (2) is shown in Fig. 2, where $t_g > t_L$ to optimize the laser energy^[11]. In Fig. 2, the continuous line is the simulation result when the laser pulse width is ignored and the DOV is $t_g c/2$. The dash line represents the simulation result when the laser pulse width is considered, and the DOV is $(t_g + t_L)c/2$. Based on the continuous line, the DOV is expanded by $t_L c/2$ and the intensity of the echo signal acquired from $R + (t_g - t_L)c/2$ to $R + t_g c/2$ rapidly declines with range. The energy profile of the dash line can evidently be divided into three parts: a head signal, a body signal, and a tail signal.

The experiment is designed as schematically illustrated in Fig. 3(a) to prove the EBE. A planar surface with depth distribution is chosen as a target. If the planar surface is not perpendicular to the imaging system in the direction of the optical axis, the head, body, and tail zones caused by the EBE can all be projected on the image plane to form a 2D image. In the image, the gray-scale value of each pixel is proportional to the integral of the product of the returned laser pulse irradiance within the instantaneous field of view of the pixel and the camera gain, and thus the 2D gray image can represent the energy profile under the EBE. In the experiment, a planar ground is selected as a target; its 2D image slice is shown in Fig. 3(b), in which only the region of interest could be imaged. In terms of this characteristic, the image slice can be divided into a viewing area and a blind area. The viewing area is formed by an echo signal from the ground. Figure 3(c) is the 3D intensity plot of Fig. 3(b), whereas Fig. 3(d) gives the plot of the row average value. Apparently, gray rising and falling parts occur on both sides of the viewing area in the depth direction. Figure 3(e) is the simulation result under the same temporal parameters as those in Fig. 3(d), in which the shape of the laser pulse is Gaussian, not rectangular. The experimental results are consistent with the simulation results, and the experiment illustrated in Fig. 3 well proves and reflects energy distribution under the EBE.

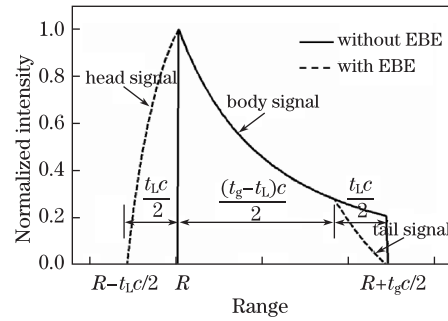


Fig. 2. Energy profile of the EBE.

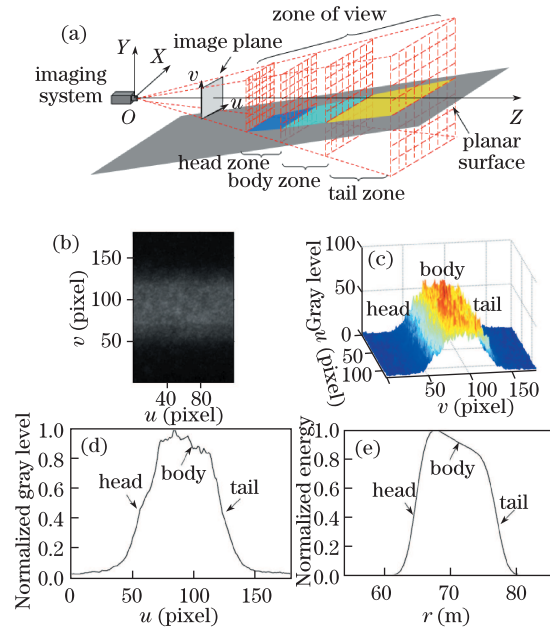


Fig. 3. (a) Spatial scheme of the EBE; (b) image slice under the EBE; (c) 3D intensity plot of panel (b); (d) row average value plot of panel (b); (e) simulation result. $\tau=440$ ns, $t_g=80$ ns, $t_L=20$ ns.

According to the energy profile of the EBE in Fig. 3, the viewing area under the EBE can be divided into a head zone, a body zone, and a tail zone. In the body zone, echo signals of targets in the field of view are all received by the imaging system, except atmospheric attenuation, whereas in the head and tail zones, only parts of the target signals are received so that targets in the two zones are relatively difficult to observe and identify. To investigate the impact of the EBE on targets, we performed the experiment described in Fig. 4 on a foggy night with all road lamps off. Figure 4(a), which is imaged in daytime, is the experimental scene in which persons T1 and T2 are positioned at 200 and 260 m, respectively. Figures 4(b)–(d) are image slices under different laser pulse widths (800, 400, and 200 ns) but with the same gate time (1340 ns) at the delay time of 660 ns. Figure 4(e) is the ratio curve of E_r/E_s based on Eqs. (2) and (3). Atmospheric backscattering is the main noise under foggy conditions with low visibility, and thus the ratio of E_r/E_s is approximately the signal-to-noise ratio (SNR) of the imaging system^[8]. In Fig. 4(e), when the laser pulse width is narrowed, the head and tail zones

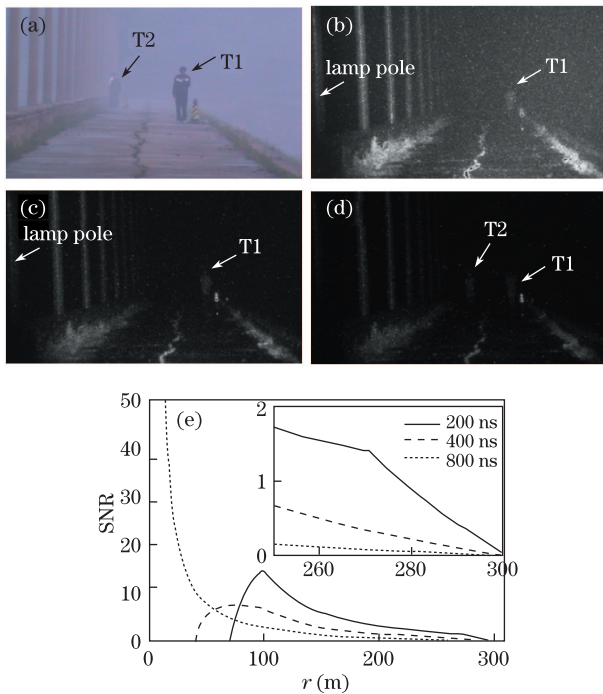


Fig. 4. Impact of the EBE on target detection. (a) Experimental scene; (b)–(d) image slices under different laser pulse widths; (e) simulation result. $\tau=660$ ns, $t_g=1\ 340$ ns.

are suppressed and the SNR increases due to the decrease in the range integral under a small t_L . The experimental results of Figs. 4(b)–(d) also demonstrate this. The lamp pole denoted in Fig. 4(b) is at 50 m. In the experiment, the pole appears in the head zone of Fig. 4(b), weakens in the head zone of Fig. 4(c), and disappears in the head zone of Fig. 4(d), which coincide with the simulation results illustrated in Fig. 4(e). Similarly, for person T2, the person appears in the tail zones of Figs. 4(b) and (c) and cannot be observed due to low SNR, but it can be detected in Fig. 4(d) due to the high SNR under the narrowed laser pulse width.

The experimental results illustrated in Figs. 3 and 4 demonstrate that the EBE has two major consequences: one is that EBE introduces two zones on both sides of the viewing area — a head zone and a tail zone that have the same depth $t_L c/2$; the echo signals of targets in these zones are only partly collected by the system. Second, the EBE introduces serious atmospheric backscattering under a large laser pulse width and decreases SNR in bad weather conditions. In addition, Fig. 4 also demonstrates that the EBE can be controlled by modifying the laser pulse width. The EBE is further enhanced with large head and tail zones when the laser pulse width is enlarged. In contrast, it is suppressed with small head and tail zones when the laser pulse width is narrowed. These results are valuable to active range-gated imaging appli-

cations. In 2D observations based on active range-gated imaging^[6,8], targets in the head and tail zones are easily missed, thereby requiring that the targets of interest be located in the body zone; furthermore, in bad weather conditions, t_L should be narrowed reasonably to reduce atmospheric backscattering. In 3D imaging based on active range-gated imaging, temporal parameters of the pulsed laser and the camera gate according to its imaging mechanism should be established. In 3D imaging based on depth scanning (time slicing)^[1,7], shorter laser pulses are needed under limited gate time to suppress the EBE and increase its depth accuracy. In gain-modulated 3D active imaging^[3,5], 3D reconstruction is realized based on the gray information of the body zone, and thus the laser pulse width should be much smaller than the gate time to narrow head and tail zones and enlarge the body zone. 3D range-gated imaging with super-resolution depth mapping^[2] and flash trajectory imaging^[9] are essentially both realized by the EBE. The results of the present study can help optimize the EBE and its temporal parameters, especially in bad weather conditions.

In conclusion, we present analytical formulas and experimental proof of the range-gated EBE and investigate its impact on target detection. The EBE impacts the energy profile of the DOV and weakens SNR under bad weather conditions. However, it can be controlled by adjusting the laser pulse width. These results are beneficial to active range-gated imaging, especially for its applications in 3D imaging.

References

1. J. Busck and H. Heiselberg, *Appl. Opt.* **43**, 4705 (2004).
2. M. Laurenzis, F. Christnacher, and D. Monnin, *Opt. Lett.* **32**, 3146 (2007).
3. C. Jin, X. Sun, Y. Zhao, Y. Zhang, and L. Liu, *Opt. Lett.* **34**, 3550 (2009).
4. C. W. Lamberts, *Appl. Opt.* **15**, 1284 (1976).
5. X. Zhang, H. Yan, and Q. Zhou, *Chin. Opt. Lett.* **9**, 061101 (2011).
6. C. S. Tan, G. Seet, A. Sluzek, and D. M. He, *Opt. Laser Eng.* **43**, 995 (2005).
7. J. Busck, *Opt. Eng.* **44**, 116001 (2005).
8. X. W. Wang, Y. Zhou, S. T. Fan, J. He, and Y. L. Liu, *Chin. Phys. Lett.* **27**, 094203 (2010).
9. X. Wang, Y. Zhou, S. Fan, J. He, and Y. Liu, *Opt. Lett.* **36**, 364 (2011).
10. L. F. Gillespie, *J. Opt. Soc. Am.* **56**, 883 (1966).
11. X. Wang, Y. Zhou, S. Fan, Y. Liu, and H. Liu, *Proc. SPIE* **7382**, 738211 (2009).
12. O. Steinvall, H. Olsson, and G. Bolander, *Proc. SPIE* **3707**, 432 (1999).
13. R. L. Espinola, E. L. Jacobs, C. E. Halford, R. Vollmerhausen, and D. H. Tofsted, *Opt. Express* **15**, 3816 (2007).